processes

MDPI

Article

Investigation of Contact Characteristics and Sealing Performance of Metal Seals in All-Metal Angle Valves

Qingyan Yang * and Yifan Wu

School of Mechanical and Electrical Engineering, Anhui Jianzhu University, Hefei 230601, China; wuyifan88@stu.ahjzu.edu.cn
* Correspondence: yangqingyan@ahjzu.edu.cn

Abstract: The sealing performance of metal seals in all-metal angle valves significantly affects their reliability and the safety of the entire fluid system. This study investigates a DN40 all-metal angle valve, analyzing the contact characteristics between the sealing ring and valve head cone surface, focusing on microscopic surface morphology. Finite element analysis and laboratory experiments were conducted on sealing rings with surface roughness values of 1.6 μm, 0.4 μm, and 0.2 μm. Additionally, leakage rates were measured experimentally to verify the model's accuracy. The results show that reducing surface roughness to 0.2 μm lowers the valve's leakage rate to 1.28×10^{-11} Pa·m^3/s, meeting ultra-high vacuum requirements. Compared to 0.4 μm, the leakage rate of 0.2 μm was reduced by 45.9%. The sealing performance of the 1.6 μm metal sealing ring was relatively poor and failed to meet ultra-high vacuum requirements. These findings align well with theoretical predictions. Further analysis revealed that lower surface roughness increases the effective contact area between the sealing ring and valve head cone, reducing leakage and improving overall sealing efficiency. These results suggest that optimizing surface roughness in sealing ring design can enhance valve performance, improving reliability and efficiency in industrial applications, particularly in vacuum systems and high-performance fluid control.

Keywords: elastic metal sealing; surface roughness; finite element analysis; leakage rate; sealing performance

check for updates

Received: 6 February 2025
Revised: 4 March 2025
Accepted: 6 March 2025
Published: 25 March 2025

Citation: Yang, Q.; Wu, Y. Investigation of Contact Characteristics and Sealing Performance of Metal Seals in All-Metal Angle Valves. *Processes* **2025**, *13*, 968. https://doi.org/10.3390/pr13040968

Copyright: © 2025 by the authors. Licensee MDPI, Basel, Switzerland. This article is an open access article distributed under the terms and conditions of the Creative Commons Attribution (CC BY) license (https://creativecommons.org/licenses/by/4.0/).

1. Introduction

The angle valve, as a common fluid control device, plays a crucial role in industrial production and fluid pipeline systems. It is sealing performance that directly determines the operational efficiency and safety of the system. With their sealing structure, metal sealing rings have become one of the most widely used sealing materials due to their superior sealing performance, as well as notable features such as high temperature resistance and corrosion resistance [1,2]. These characteristics make them highly favored in applications involving high temperatures, high pressures, and corrosive media. However, despite the widespread use of metal sealing rings in angle valves, their leakage characteristics still present certain challenges. Leakage issues not only have the potential to cause energy waste and environmental pollution but may also lead to safety accidents, posing significant risks to the operation of the system [3]. Therefore, in-depth research on the leakage characteristics of metal sealing rings in angle valves is of significant importance not only for improving sealing designs and enhancing system efficiency but also for increasing the overall safety of the system [4,5].

Metal sealing rings are commonly classified into various types, including C-rings, O-rings, B-rings, and W-rings, based on their cross-sectional configurations [6]. Each type exhibits distinct properties and performance characteristics due to the inherent differences in their geometrical design [7]. In the performance of sealing elements and optimization of metal sealing structures, Kim et al. [8] employed a real-coded genetic algorithm to optimize the design of O-ring seals, aiming to improve their elastic recovery. The performance of these optimized seals was validated through experimental testing, demonstrating enhanced sealing efficiency. Similarly, Gao et al. [9] developed a set of deformation coordination equations for B-ring seals, identifying key factors that significantly influence their sealing capabilities. Cheng et al. [10] utilized finite element analysis to simulate the mechanical behavior of combined sealing rings under varying load conditions, further exploring how structural parameters affect their overall sealing performance. Y. S. Lee et al. [11] optimized the O-ring structure using a modified genetic algorithm (RCGA) to improve stress distribution and compression–rebound characteristics. Yan Hui [12] identified sealing gap height as a key factor affecting the leakage characteristics of O-rings and proposed a leakage model based on the parallel plate formula. Blanton et al. [13] analyzed the impact of parameters such as medium pressure and temperature on the leakage of silver-plated spring C-type sealing rings. Tsujikawa H et al. [14] tested the leakage of C-type seals with different coating materials, finding that WC-Co-coated C-type seals exhibited excellent sealing performance. A leakage rate calculation model and thermo-mechanical coupling analysis were used to assess the failure probability of the sealing ring and perform parameter sensitivity analysis. Huang et al. [15] investigated an improved O-ring with a metal core and analyzed its sealing performance under high-pressure conditions. The study found that the reinforced O-ring experienced less deformation under pressure, leading to improved sealing performance. El Bahloul et al. [16] utilized finite element analysis (FEA) to investigate the impact of external loads on sealing performance and calculated the variations in contact stress and equivalent stress. The findings provide valuable insights for the design of sealing rings and composite sealing structures.

A large number of studies have shown that the leakage rate is influenced by various factors such as contact stress, contact area, contact width, and surface morphology between the contact surfaces. Gu et al. [17] examined the influence of surface roughness and wettability on the leakage rate of static seals. The study revealed that an increase in contact pressure leads to a reduction in leakage rate, while an increase in surface roughness results in a higher leakage rate. Wu et al. [18] analyzed the effect of the microscopic morphology of metal sealing contact surfaces on leakage rate. The results indicated that as surface roughness increases, the leakage rate follows an exponential growth trend. Dai et al. [19] investigated the effect of surface texture (grinding direction) on leakage and found that grinding marks parallel to the leakage direction increase the leakage rate, while grinding marks perpendicular to the leakage direction reduce leakage. Nurhadiyanto and Gong [20,21] used contact stress as an important parameter for evaluating leakage rates in gasket optimization design. Persson et al. analyzed how the microscopic actual contact area changes with variations in sliding velocity and nominal contact pressure, predicting that in most cases, the contact area is linearly related to the load [22,23]. They also investigated the effect of contact stress on the leakage behavior of metal sealing rings [24]. Additionally, Haruyama et al. explored the relationship between contact width and leakage rate, finding that an increase in contact width significantly reduces the leakage rate [25].

Existing studies on metal sealing performance primarily focus on structural optimization, material properties, and the influence of surface morphology on leakage rates. While efforts have been made to optimize sealing parameters and analyze contact pressure distribution and elastic recovery, research remains largely constrained to macroscopic

assessments, overlooking the role of microscopic surface contact deformation. Moreover, the evolution of equivalent stress distribution, contact stress variations, and real contact area under different operating conditions remains inadequately explored, necessitating further investigation.

To address these gaps, this study integrates theoretical modeling, finite element analysis (FEA), and experimental validation to systematically examine metal sealing mechanisms. The key objectives include: (1) developing an analytical model incorporating microscopic contact mechanics to quantify surface roughness effects; (2) employing FEA to assess the evolution of stress distribution and real contact area under varying roughness conditions; and (3) designing a sealing performance testing apparatus to evaluate mechanical and leakage characteristics under applied loads. By correlating experimental findings with numerical simulations, this study aims to elucidate the role of microscopic surface features in sealing efficiency and provide a theoretical foundation for optimizing sealing design and reliability in engineering applications.

2. Mechanism Analysis of Metal Seal Ring Sealing and Finite Element Model Development

2.1. Mechanism Analysis of Metal Seal Ring Sealing

The metal sealing ring studied in this paper is a key component in the ultra-high vacuum angle valve. Its sealing structure, as shown in Figure 1, consists of major components such as the valve head, O-ring, and valve body. The specific structural parameters of the metal sealing ring are listed in Table 1. This sealing structure successfully converts and amplifies the radial force and the normal force acting on the conical surface through a carefully designed conical geometry, thus significantly enhancing the sealing performance efficiency and reliability under relatively low axial load conditions.

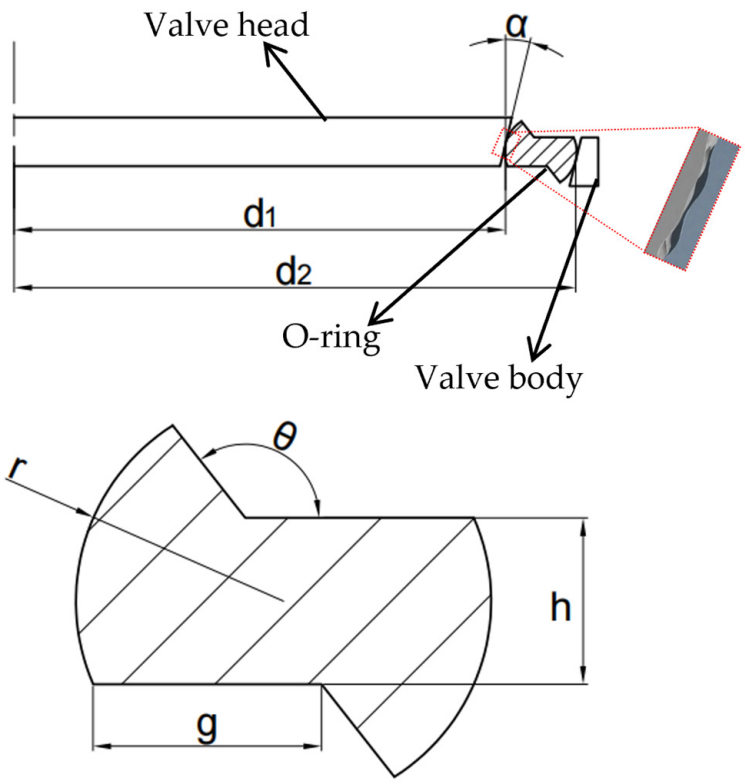


Figure 1. Structural diagram of the metal sealing ring.

Table 1. Structural parameters of the metal sealing ring.

Structural Parameters	Parameter Values	Units
Valve head half apex angle α	11.15	°
Inner diameter of the sealing ring d_1	37.1	mm
Outer diameter of the sealing ring d_2	41.1	mm
Arc radius r	1	mm
Plane height h	0.65	mm
Plane width g	1.1	mm
Chamfer angle θ	132.9	°

The sealing ring adopts a line-contact sealing design with double arc surfaces and double conical surfaces. This design forms a reliable sealing performance through the extrusion effect. The line contact between the double conical and double arc surfaces ensures good conformity at the sealing position. However, in practical applications, due to the elastic–plastic deformation of the material, line contact often cannot form a continuous contact surface at the sealing position. Under the action of axial compression, the sealing contact area undergoes plastic deformation, forming an annular closure sealing band with a certain width. The existence of this sealing band ensures effective sealing functionality and plays a crucial role in the stability and durability of the sealing performance.

2.2. Development of the Integrated Sealing Model

The material of the O-ring metal seal used in this study is the deformed high-temperature alloy GH4169. The material properties [26] were obtained from relevant literature, as listed in Table 2. In the annealed state, the hardness is 200–220 HB, and in the age-hardened state, it ranges from 300–350 HB. The elongation is between 30 and 40%. The main composition consists of nickel (50–55%), chromium (17–21%), and molybdenum (2.8–3.3%). GH4169 possesses excellent high-temperature strength, oxidation resistance, and ductility, making it widely used in aerospace and other high-performance applications.

Table 2. Basic mechanical properties of GH4169.

Temperature T/K	Tensile Strength σ_b/MPa	Yield Strength σ_s/MPa	Elastic Modulus E/GPa
293	1465	1265	203

2.2.1. Contact Pair Setup

The analytical model in this paper takes the inclined conical surfaces of the valve head and conical hole as the primary contact surfaces, and the arc surface of the sealing ring is set as the contact surface, ensuring that the mechanical behavior of key areas can be accurately simulated and analyzed. In this study, a friction coefficient of 0.15 is selected, and the contact model algorithm employs an enhanced Lagrangian method. The choice of this friction coefficient is based on the research presented in reference [27], where this setting was applied to simulate the sealing performance of the GH4169 sealing ring. This value has been widely used in similar finite element analysis models to simulate the sealing contact behavior.

2.2.2. Model Simplification and Structured Mesh Division

Given the symmetry of the model in terms of structural design, load distribution, and boundary conditions about the centerline axis, a 2D planar sealing model was constructed using the Design Modeler module to optimize computational resources and improve the convergence efficiency of the solution. The geometric behavior was set to an axisymmetric form to achieve simplified modeling and efficient computation. While a full 3D analysis

would provide a more detailed representation, the computational resources required for such an analysis would result in excessive computation times, exceeding the capacity of the available equipment and the project's time constraints. The 2D axisymmetric model was deemed sufficient, as it accurately captured the primary mechanical characteristics of the sealing ring under actual operating conditions. Comparative tests with 3D analysis showed that the error in stress values was within an acceptable range of ±0.2%. Therefore, the 2D axisymmetric model was chosen for this study, balancing computational efficiency with the need for accuracy.

When determining the mesh size of the model, a sensitivity analysis needs to be performed initially [28]. Since this study primarily focuses on analyzing the stress distribution of the metal sealing ring, and considering that the sealing ring has relatively small dimensions with a complex stress state, a finer mesh is required to accurately capture the mechanical behavior. Due to the intricate stress distribution within the sealing ring, insufficient mesh refinement may result in significant local stress variations, affecting the accuracy of the simulation results. Therefore, an appropriate mesh density must be ensured to balance computational efficiency and result accuracy.

Based on the actual dimensions of the model and engineering experience, the initial mesh sizes for the valve head, conical hole, and sealing ring are set to 0.3 mm, 0.3 mm, and 0.15 mm, respectively. After applying the constraints and loads, the first finite element calculation is performed, and the maximum equivalent stress (von Mises) on the contact surface is recorded. Subsequently, the mesh size is gradually reduced by a certain proportion (each time reducing by 1/8 of the original size), and the finite element calculation is repeated, recording the maximum equivalent stress for each iteration. To ensure the reliability of the results, the convergence criterion is set such that when the variation in the maximum equivalent stress between two consecutive iterations falls below 3%, the mesh is considered sufficiently refined. The smaller mesh size obtained under this criterion is selected as the final mesh size for subsequent simulation calculations.

Based on the sensitivity analysis above, the final mesh sizes for the cone tip, cone hole, and sealing ring were determined to be 0.1 mm, 0.1 mm, and 0.05 mm, respectively. Additionally, to improve the accuracy of the computational results, a threefold mesh refinement was applied to the beveled and curved edges in the structural contact region, enabling point-to-point contact. This refinement was aimed at constructing a reasonable two-dimensional finite element mesh structure. The mesh division for the local region is shown in Figure 2.

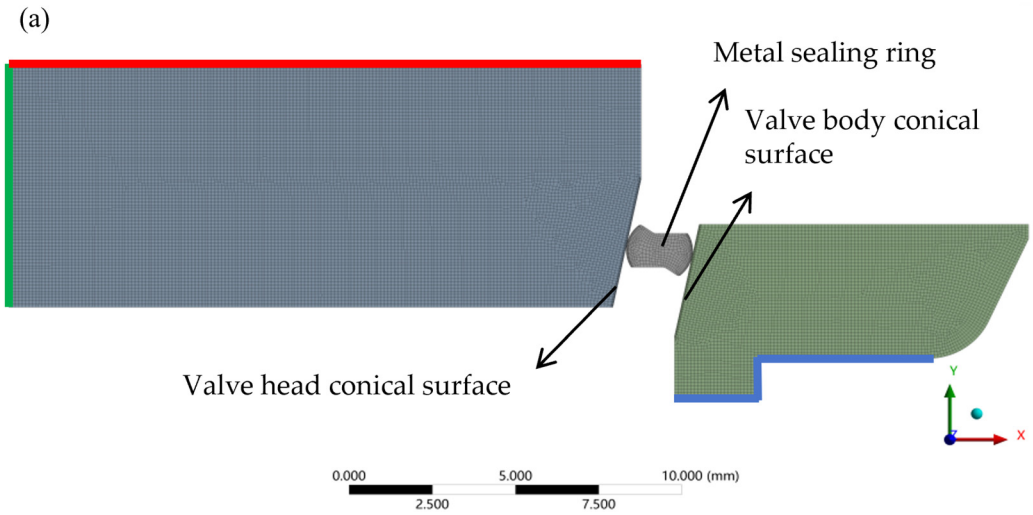


Figure 2. *Cont.*

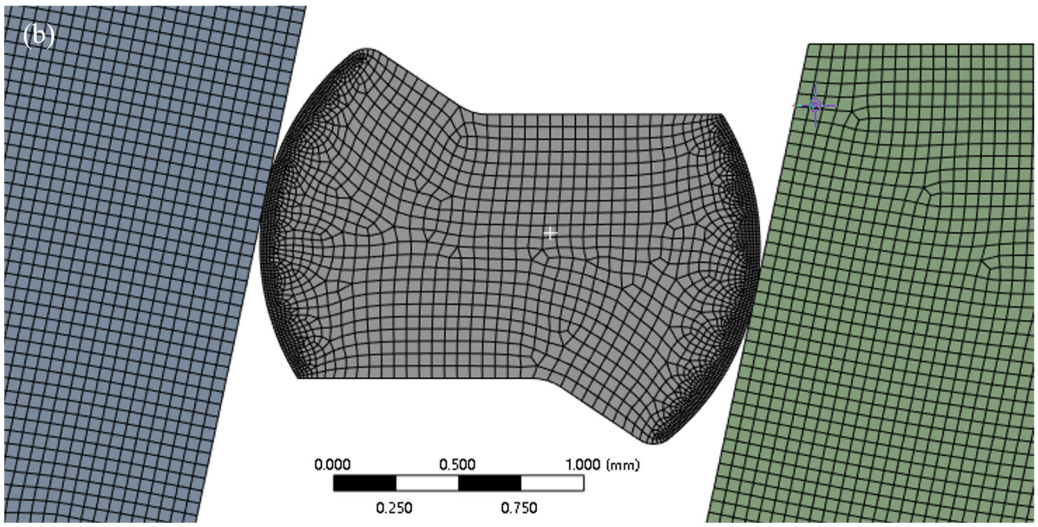


Figure 2. Finite element simulation mesh model: (**a**) overall mesh model; (**b**) local mesh model.

Due to the potential for local yielding of the sealing ring during operation, the sealing structure typically relies on localized plastic deformation to achieve effective sealing. Therefore, the contact stress of the overall structure becomes a critical parameter in determining the sealing performance.

2.2.3. Boundary Conditions

Considering the structural and loading symmetry about the central axis, the following symmetric boundary conditions are applied to the model: a fixed constraint is applied to the bottom edge of the tapered hole, as shown in the blue section of Figure 2a; the left edge of the valve head is constrained in all degrees of freedom except for displacement in the Y direction, as indicated by the green section of Figure 2a; and the cross-section of the sealing ring is constrained in the Z-direction displacement and in the rotational degrees of freedom about the X and Y axes, as represented by the gray mesh section in Figure 2b. Additionally, a displacement load is applied to the upper side of the valve head, shown in red in Figure 2a, to simulate the downward motion of the tapered valve stem during the vacuum valve's actual closing process.

According to the pressure test experiment on the same DN40 all-metal angle valve reported in reference [29], the tapered head is subjected to a vertical downward load of 2.2 MPa when the valve is closed. Considering potential plastic deformation in the sealing contact region, the Large Deflection function is enabled for analysis.

3. Simulation of Microscopic Surface Topography and Development of a Preloading Model

3.1. Fractal Theoretical Analysis for the Construction of a Three-Dimensional Rough Surface Model

The components, when considered as a whole and resembling a specific geometric form, are referred to as fractals. This fractal characteristic is of significant importance when describing complex surface topographies. The rough peaks on the surface of metal sealing rings typically follow a Gaussian distribution, and the microscopic rough surface exhibits prominent self-affine characteristics. A self-affine surface refers to a surface whose statistical properties remain invariant under a scale transformation, meaning that the surface exhibits the same roughness at different scales, but the magnitude of roughness varies with the scale of observation. These self-affine features make it challenging for traditional simple geometric models to accurately represent the surface morphology. The introduction of the multivariable Weierstrass–Mandelbrot (W-M) model effectively overcomes this limitation.

By incorporating complex mathematical descriptions, the W-M model offers a more accurate representation of rough surfaces, capturing the microscopic features of three-dimensional rough surfaces with greater precision.

When characterizing the three-dimensional rough surface morphology, the modified two-variable Weierstrass–Mandelbrot (W-M) function can be used. This function effectively simulates the self-affine characteristics of three-dimensional rough surfaces, making it an important tool for studying complex rough surface topography. The mathematical expression of the W-M function is as follows [30,31]:

$$z(x,y) = L(G/L)^{Ds-2}(\ln\delta/W)^{1/2}\cdot\sum_{m=1}^{W}\sum_{n=0}^{n_{\max}}\delta^{(Ds-3)n}\cdot\{\cos\theta_{m,n}-\cos\left\{2\pi\delta^{n}\left(x^{2}+y^{2}\right)^{1/2}/L\cdot\cos[\arctan(y/x)-\pi m/W]+\theta_{m,n}\right\}\} \quad (1)$$

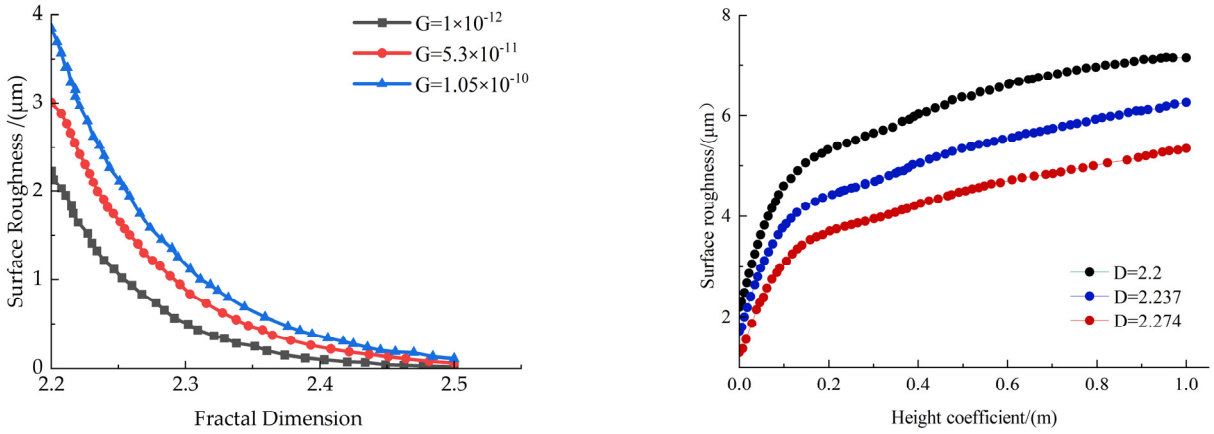
In Equation (1), $z(x,y)$ represents the random surface height; L is the total length of the sample; G is the scale factor for the response height; D_s is the fractal dimension, with a range of 2 to 3; δ is the scaling factor for frequency density; W represents the number of frequency wave superimpositions; $n_{\max}$ is the maximum value of n, defined as $n_{\max}$ = int[log(L/L_s)/logδ]; L_s is the minimum identifiable length, which is taken as 1×10^{-5} m; and $\theta_{m,n}$ is the parameter term that introduces randomness.

The morphological characteristics of the simulated rough surface determine the fractal dimension D_s and scale factor G, which characterize the fractal properties of the rough surface. These parameters serve as key indicators for describing surface features, reflecting geometric complexity and height variation patterns while remaining unaffected by changes in resolution. Therefore, by establishing a geometric leakage model based on fractal characteristics, determining the corresponding fractal dimension D_s and scale coefficient G under different roughness conditions allows the geometric model to more accurately simulate the actual rough surface morphology.

As shown in Figure 3, the relationship curves between the surface roughness, fractal dimension, and scale coefficient at a specific cross-section are presented. The figure indicates a certain correlation between the surface roughness, fractal dimension D_s, and scale coefficient G [32,33]. When the scale coefficient G is fixed, an increase in the fractal dimension D_s leads to a decreasing trend in surface roughness, which gradually stabilizes. Conversely, when the fractal dimension D_s is fixed, an increase in the scale coefficient G initially causes a rapid rise in surface roughness, followed by a gradual deceleration in the growth rate. Therefore, by appropriately setting the specific values of D_s and G, point cloud data corresponding to different roughness levels can be generated to meet specific research needs.

3.2. Surface Observation Experiment of Sealing Ring Specimens

To ensure the scientific rigor and reliability of this study, as well as the accuracy of the simulation results, a surface morphology observation experiment was conducted to examine the surface characteristics of three metal sealing rings with different roughness levels. As shown in Figure 4, the three metal sealing rings used in the microscopic surface morphology simulations are displayed from left to right as Specimen 1, Specimen 2, and Specimen 3. These specimens were analyzed to investigate the effects of surface roughness on sealing performance.



(**a**) (**b**)

Figure 3. Relationship between fractal dimension, scale coefficient, and surface roughness. (**a**) Relationship between fractal dimension and surface roughness. (**b**) Relationship between scale coefficient and surface roughness.

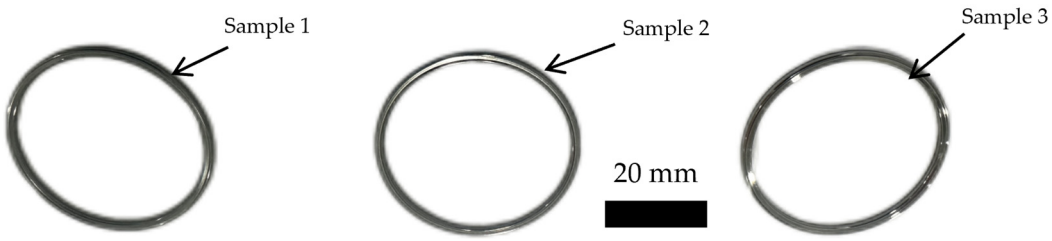


Figure 4. Metal sealing ring samples with three different surface topographies.

As shown in Figure 5, the experimental procedure for observing the surface morphology of Specimen 1 using a VR-3000 machine vision three-dimensional profilometry system is presented. This system accurately measures and records the surface roughness characteristics of the metal sealing rings. The purple-red area in the figure represents the portion selected from the scanned region of the specimen that is suitable for analysis using the surface morphology analysis system. The analysis is then conducted, and relevant information regarding the surface morphology of the specimen is obtained.

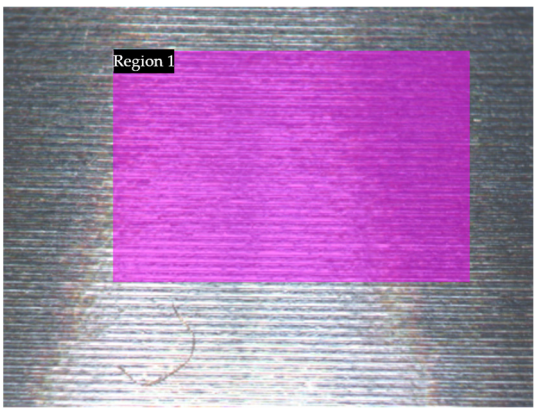


Figure 5. Observation of surface topography using a 3D profiling system.

A three-dimensional profilometry system was employed to individually measure the three sealing ring specimens, obtaining their corresponding scale coefficient, fractal dimension, and surface roughness. The results are summarized in Table 3.

Table 3. Experimental results of surface observation for sealing ring specimens.

Experimental Sample	D_S	G/m	Ra/μm
Sample 1 (sealed)	2.4	5.1×10^{-11}	1.6
Sample 2 (sealed)	2.42	2.15×10^{-12}	0.4
Sample 3 (sealed)	2.44	1.27×10^{-12}	0.2

3.3. Simulation of Rough Surface Point Cloud Dataset Based on Fractal Theory

To reduce computational complexity and improve computational efficiency, the contact area between the sealing ring and the valve body was discretized into small elements (20 μm). Therefore, a planar surface morphology model was established, without considering the variation in the sealing ring's rough surface along the circumference. Based on the Weierstrass–Mandelbrot (W-M) function, a metal rough surface model was constructed in MATLAB R2021b. By setting different surface roughness parameters, corresponding three-dimensional rough surface models were generated, along with surface point cloud data under various roughness conditions. As shown in Figure 6, the simulated surface morphology of the contact area is presented for three different roughness levels.

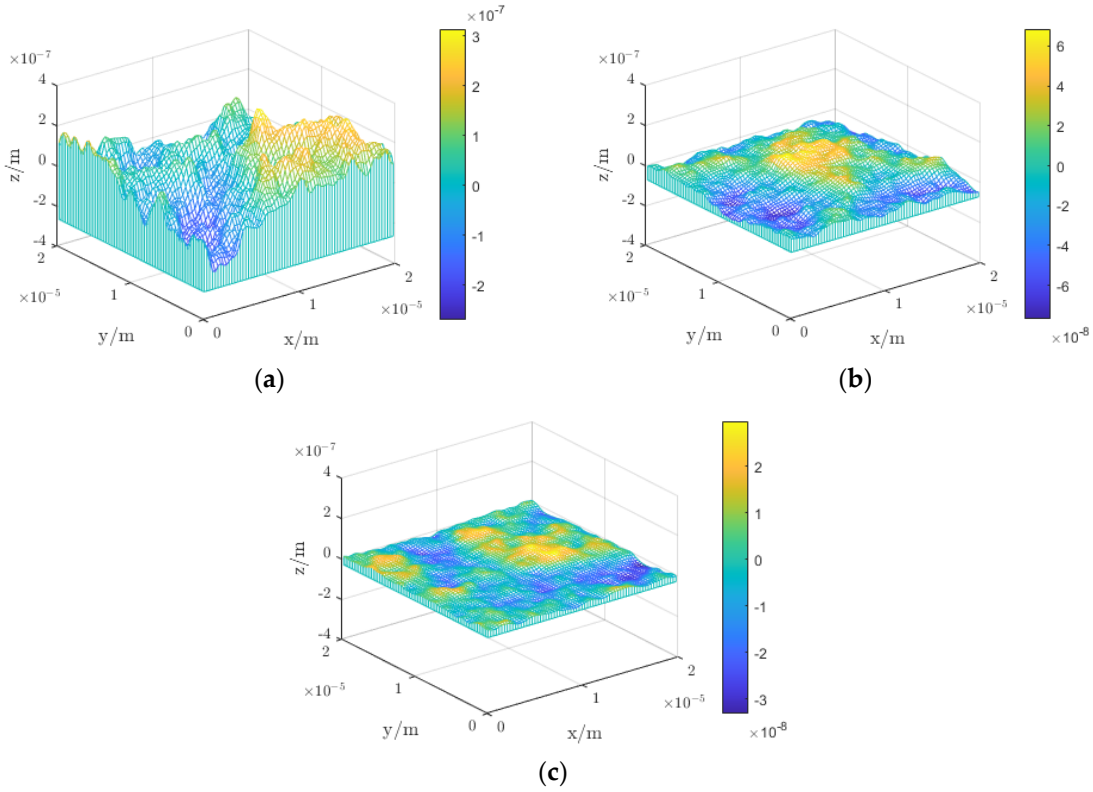


Figure 6. Surface topography simulation under different roughness conditions: (**a**) microscopic surface simulation of Ra 1.6 μm; (**b**) microscopic surface simulation of Ra 0.4 μm; (**c**) microscopic surface simulation of Ra 0.2 μm.

The MATLAB simulation provides an intuitive visualization of surface morphology variations under different roughness conditions. These simulation results provide fundamental data for investigating the influence of rough surface characteristics on sealing performance. Additionally, the generated point cloud data can be directly applied to contact mechanics analysis, laying a solid foundation for subsequent research.

3.4. Surface Reconstruction Based on NURBS Modeling

Following Versprille's Non-Uniform Rational B-Splines (NURBS) method, a modeling approach based on NURBS was employed to reconstruct the rough surface of the metal sealing ring. The mathematical formulation is given as follows [34]:

$$p(u,v) = \frac{\sum_{i=0}^{m}\sum_{j=0}^{n} N_{i,k(u)} N_{j,l(u)} w_{ij} p_{ij}}{\sum_{i=0}^{m}\sum_{j=0}^{n} N_{i,k(u)} N_{j,l(u)} w_{ij}} \quad (2)$$

where $p(u,v)$ represents the surface height, p_{ij} denotes the control vertices of the surface, and m, n are the orders of the NURBS curves in the u and v parametric directions, respectively. The indices $I = 0, 1, \ldots, m$ and $j = 0, 1, \ldots, n$ correspond to the control vertex weighting factors. k and l are the degrees of the NURBS curves in the u and v directions, while $N_{i,k(u)}$ and $N_{j,l(v)}$ represent the basis functions of the NURBS curves.

Based on the NURBS surface modeling approach, the point cloud data obtained from experiments were imported into the 3D design software CATIA V5 to reconstruct the solid rough surface model. This method accurately represents complex surface morphology, ensuring high accuracy and realism in the model. As shown in Figure 7, the reconstructed surface morphology of a metal sealing ring with a surface roughness of 1.6 μm is presented using the point cloud dataset.

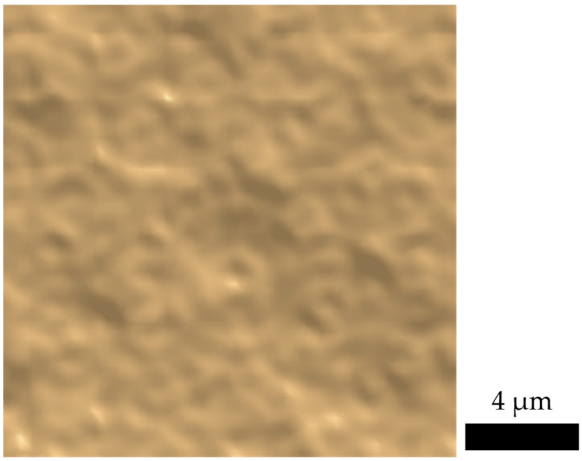


Figure 7. Simulation of surface reconstruction with a surface roughness of 1.6 μm.

3.5. Development of a Preloading Model for Microscopic Contact Regions

Relative displacement, rough surface morphology, and microscopic contact area are key indicators for characterizing contact behavior, playing a crucial role in evaluating the sealing performance of metal sealing rings. Based on these indicators, this study further explores the effect of surface roughness on sealing performance and its engineering applications.

In practical engineering applications, the surface roughness of metal sealing rings is typically significantly higher than that of the valve head taper. This roughness difference allows for a simplified analysis of sealing performance. To reduce computational complexity and improve efficiency in contact analysis, it is assumed that the sealing ring surface is rough, while the valve head taper is an idealized rigid and smooth plane. Although this assumption simplifies the actual surface conditions, practical applications have demonstrated that it maintains computational accuracy while meeting engineering requirements, thereby providing a reliable basis for the quantitative analysis of sealing performance.

Further research focused on the geometric simplification of the rough sealing ring surface to establish a preload model based on rough surface morphology. This model not only provides an intuitive description of the compression and deformation behavior of the rough surface under contact stress but also, through geometric simplifications, accurately simulates the physical characteristics of asperities on the contact surface. The preload model enables precise characterization of rough surface contact behavior, forming a robust theoretical foundation for subsequent contact performance analysis.

Moreover, the preload model effectively transforms complex surface morphology into representative geometric parameters, significantly simplifying the computation of contact stress distribution. This approach is applicable to the performance evaluation of various sealing structures and facilitates further optimization of sealing designs. This model enables detailed analysis of stress distribution and deformation behavior of rough surfaces under different loading conditions, providing insights into the influence mechanism of roughness parameters on sealing performance. As shown in Figure 8, the finite element software ABAQUS was used to simulate the deformation behavior of the microscopic surface under applied loads.

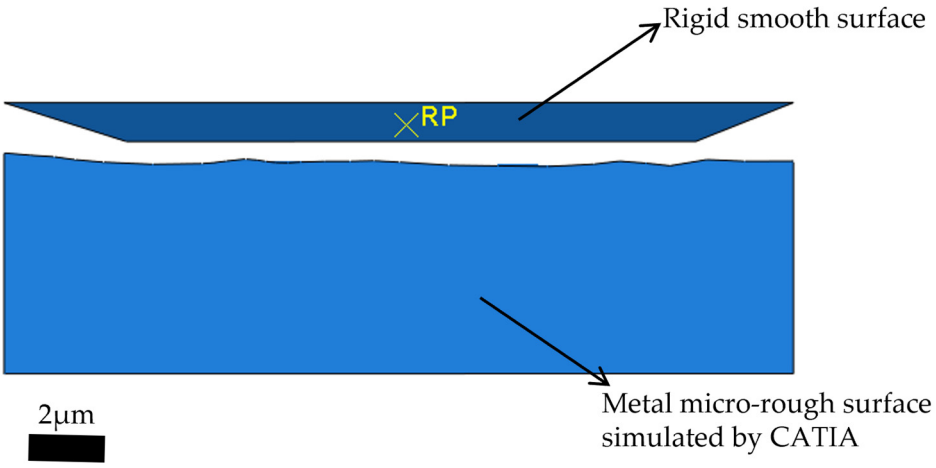


Figure 8. Micro-surface deformation simulation model under load.

In summary, considering the surface roughness of the sealing ring as the research focus and establishing a preload model through geometric processing not only offers an efficient computational approach for analyzing sealing performance but also helps address practical challenges in evaluating sealing performance under complex operating conditions. Future research can incorporate the elastic–plastic properties of different materials to further optimize the model, enhancing its applicability to more complex engineering environments.

In this study, the finite element method (FEM) was employed for numerical simulation analysis, with the contact load determined from the contact stress σ_c obtained in the overall structural analysis. The contact process was precisely modeled and solved, yielding displacement data for the deformed rough surface. These results provide critical support for the study of surface deformation characteristics.

4. Analysis of Simulation Results

4.1. Finite Element Simulation Analysis of the Sealing Region in Metal Sealing Rings

4.1.1. Equivalent Stress

In Figure 9, the von Mises stress distribution of the sealing ring under different axial loads applied to the valve head is presented. The results indicate that the equivalent stress in the metal sealing ring is symmetrically distributed about its geometric center, providing a basis for simplifying the subsequent contact stress and contact state analysis. Figure 9d

illustrates the von Mises stress distribution when an axial load of 2.2 MPa is applied to the valve head, revealing a maximum stress of 548.95 MPa in the contact region. Since this value is lower than the yield strength of the material, the metal sealing ring undergoes only elastic deformation under the given loading conditions. However, if the applied stress exceeds the yield strength, plastic deformation will occur, leading to the accumulation of irreversible deformations. This progressive plastic strain can compromise the sealing integrity, ultimately resulting in sealing failure.

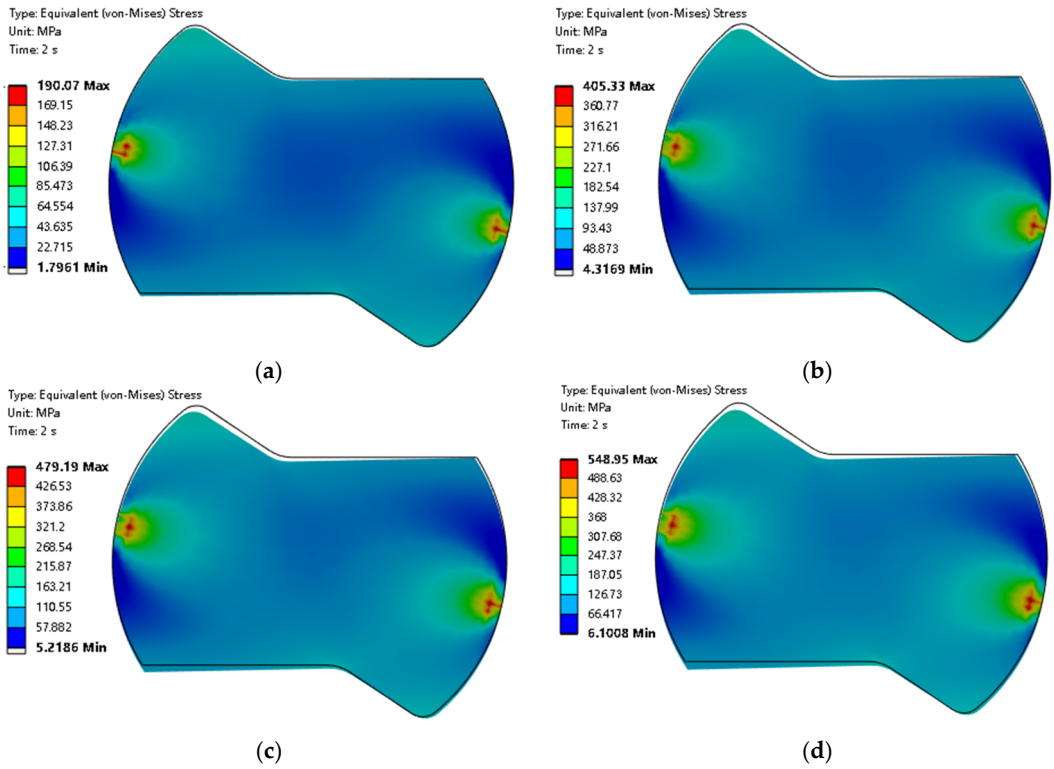


Figure 9. Von Mises stress distribution of the sealing ring at different axial loads. (**a**) Pressure load of 0.6 MPa (**b**) Pressure load of 1.4 MPa (**c**) Pressure load of 1.8 MPa (**d**) Pressure load of 2.2 MPa.

A comparison of equivalent stress distributions under different loading conditions shows that the maximum stress consistently occurs in the contact region, while the overall stress distribution remains similar. This phenomenon is attributed to the compression of the sealing ring between the valve head and the valve seat. Moreover, the maximum equivalent stress increases linearly with the axial load.

The black contour line in the figure represents the initial position of the metal sealing ring. By comparing the initial and deformed positions, it is observed that the sealing ring rotates counterclockwise around its contact point with the valve seat as the axial load increases. Furthermore, the degree of counterclockwise rotation increases with the axial load.

4.1.2. Contact Stress

Due to the symmetric stress distribution about the geometric center of the sealing ring under loading, the contact stress analysis focuses only on the contact region between the metal sealing ring and the valve head taper. This approach reduces computational resource consumption and enhances numerical convergence.

Figure 10 presents the contact stress distribution of the sealing ring under different axial loads, showing a gradient decrease from the peak at the center toward the edges. This phenomenon occurs because the axial load applied to the valve head is concentrated within

a narrow, closed annular contact band. By dividing the stress distribution into upper and lower regions at the central peak, it is observed that the upper region is wider than the lower region. This difference arises from the transition from line contact to surface contact as the sealing ring undergoes counterclockwise rotational deformation. Additionally, the slope of the stress gradient in the upper region is gentler than that in the lower region, indicating that stress values are generally higher in the upper region. This further suggests that the direction of compressive force also shifts counterclockwise during the rotational deformation of the sealing ring.

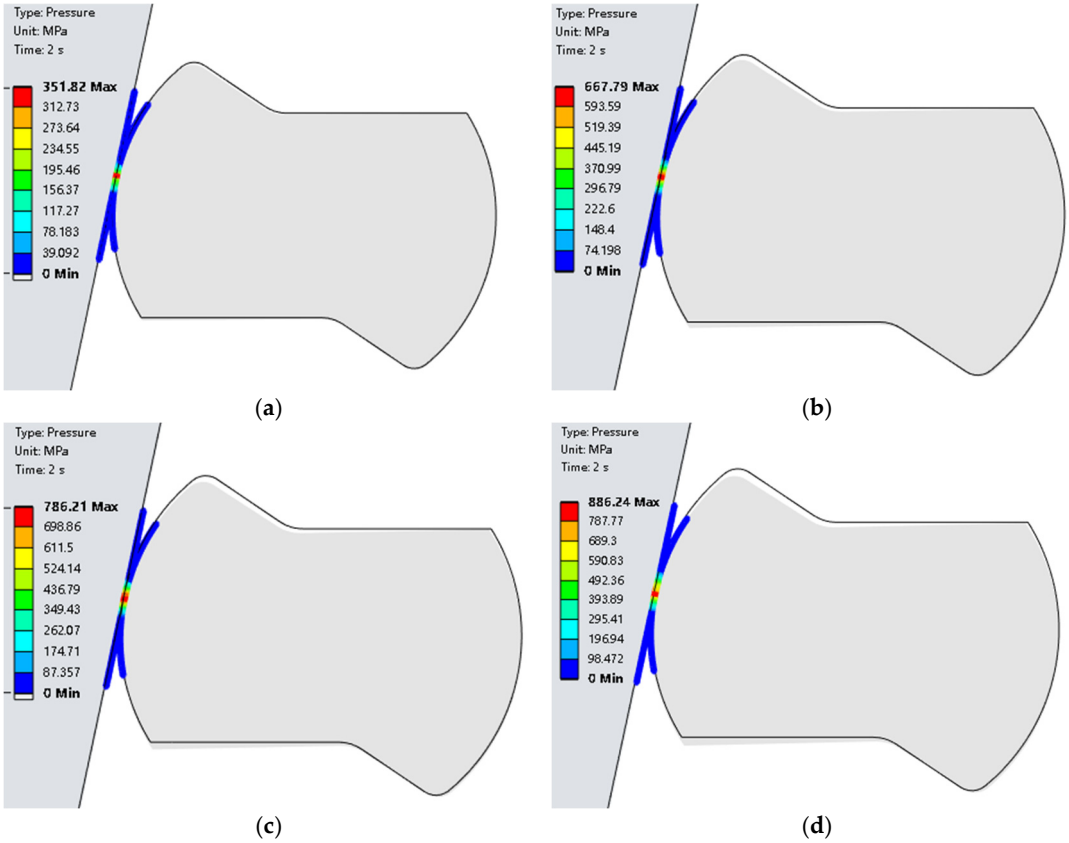


Figure 10. Contact stress distribution of the sealing ring under different axial loads. (**a**) Pressure load of 0.6 MPa; (**b**) pressure load of 1.4 MPa; (**c**) pressure load of 1.8 MPa; (**d**) pressure load of 2.2 MPa.

Figure 10d shows the von Mises stress distribution when an axial load of 2.2 MPa is applied, where the maximum stress in the contact region between the sealing ring and the valve head taper reaches 886.24 MPa. Since the maximum stress of 886.24 MPa does not exceed the yield strength of GH4169 (1265 MPa), the metal sealing ring remains in an elastic deformation state, and its structural integrity will not be compromised.

4.1.3. Contact Area

Figure 11 illustrates the contact states between the sealing ring and the valve head taper under different axial loads. Despite variations in the axial load applied to the valve head, the contact state remains nearly identical. This is because, once contact is established between the valve head taper and the sealing ring, the sealing ring undergoes counterclockwise rotation around its contact point with the valve seat during loading. Consequently, the arc surface of the sealing ring maintains line contact with the valve head taper. Due to the material properties of the metal sealing ring, elastic deformation remains minimal, resulting in negligible changes in the contact state and contact area as the axial load increases.

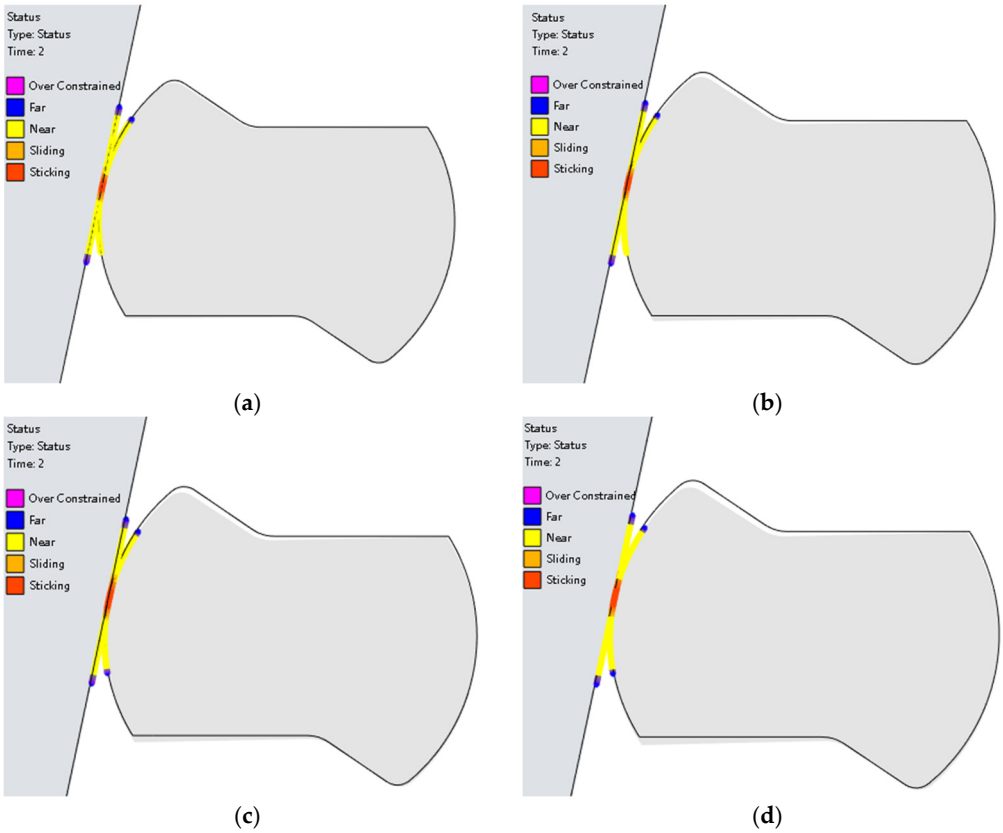


Figure 11. Contact state between the sealing ring and the valve head taper under different axial loads. (**a**) Pressure load of 0.6 MPa; (**b**) pressure load of 1.4 MPa; (**c**) pressure load of 1.8 MPa; (**d**) pressure load of 2.2 MPa.

Figure 12 presents the variation curves of equivalent stress, contact stress, and contact area under increasing axial loads at a temperature of 20 °C. The results indicate that both equivalent stress and contact stress exhibit a distinct linear growth trend with increasing axial load. This trend suggests that, within the design load range, the mechanical response of the sealing ring remains highly linear, with contact stress variations primarily driven by the increase in axial load.

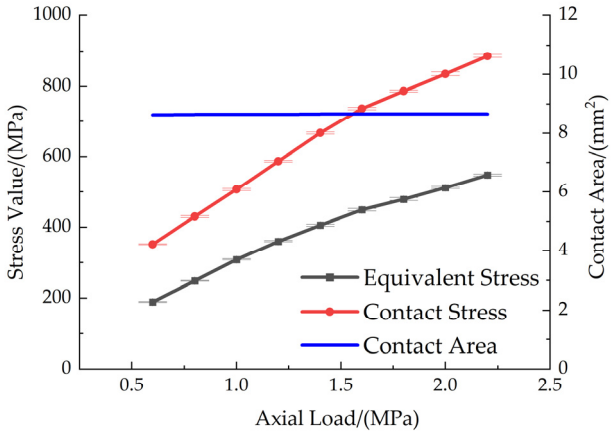


Figure 12. Variations in von Mises stress, contact stress, and contact area with axial load.

This phenomenon can be explained using contact mechanics principles. As the axial load increases, the pressure on the sealing ring's contact surface also rises, leading to a linear increase in contact stress. Simultaneously, equivalent stress, as an indicator of the overall structural stress state, also increases proportionally with the rise in contact stress.

The observed linear relationship within the design load range suggests that the sealing ring structure does not exhibit significant yielding or nonlinear deformation in this range.

The contact area plays a crucial role in determining leakage rates. Finite element simulations were conducted to obtain the variation curve of contact area during loading. The results show that, after initial contact is established between the metal sealing ring and the valve head taper, the contact area remains nearly constant. This finding implies that, when performing microscopic surface morphology simulations for the same type of sealing ring, reconstructing the rough surface may be unnecessary, thereby simplifying leakage rate calculations and improving computational efficiency.

4.2. Finite Element Simulation Analysis of Microscopic Preloading Model Results

The simulation results are shown in Figure 13. In the microscopic contact model, as the contact stress increases, the conformity between the valve head and the sealing ring surface gradually improves, significantly enhancing surface compression, which follows a distinct trend of relative displacement variation. The contact analysis results indicate that the relative displacement of the contact surface increases with increasing contact stress. However, this growth trend gradually slows down, primarily due to changes in surface roughness and load-bearing capacity during the contact process.

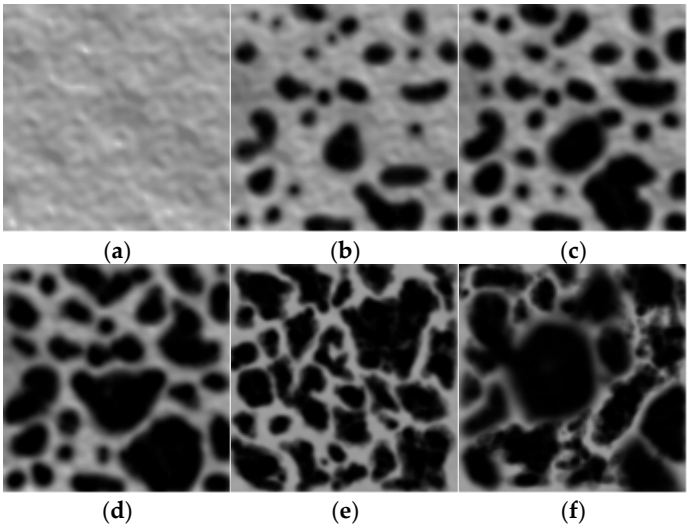


Figure 13. Deformation of rough surfaces under different loading conditions: (**a**) 1.6 μm, 0 MPa; (**b**) 1.6 μm, 300 MPa; (**c**) 1.6 μm, 600 MPa; (**d**) 1.6 μm, 886 MPa; (**e**) 0.4 μm, 886 MPa; (**f**) 0.2 μm, 886 MPa.

At the initial stage of contact, due to the relatively high surface roughness of both surfaces, the actual load-bearing area is primarily concentrated on a limited number of sharp asperities. These asperities have extremely small contact areas due to their geometric characteristics, resulting in relatively weak load-bearing capacity. As the contact stress increases, the pressure is concentrated in these localized areas, leading to a highly non-uniform stress distribution. This pressure concentration effect induces significant local deformation of the asperities, causing a rapid increase in overall axial displacement during the early stage.

This phenomenon can be explained from the perspective of contact mechanics: within the limited contact area, the applied external force is concentrated on a small number of roughness peaks, causing their contact stress to significantly exceed the material's yield strength, thereby resulting in plastic deformation or significant elastic deformation. Meanwhile, other asperities that have not yet come into contact do not contribute to the overall deformation, meaning that the initial displacement is mainly dominated by the

severe deformation of a few asperities. This stage of displacement characteristics directly reflects the initial influence of surface roughness on the contact interface.

As shown in Figure 14, which depicts the relative displacement of the rough surface under varying contact stresses, with the further increase in contact stress, more asperities on the rough surface gradually begin to bear the load, leading to expansion of the contact area and a significant enhancement in the overall load-bearing capacity of the surface. During this stage, as contact pressure is progressively distributed across more asperities, the local stress concentration effect is effectively alleviated, resulting in notable changes in the overall deformation characteristics of the rough surface. This transition manifests as a gradual deceleration in the rate of axial displacement growth.

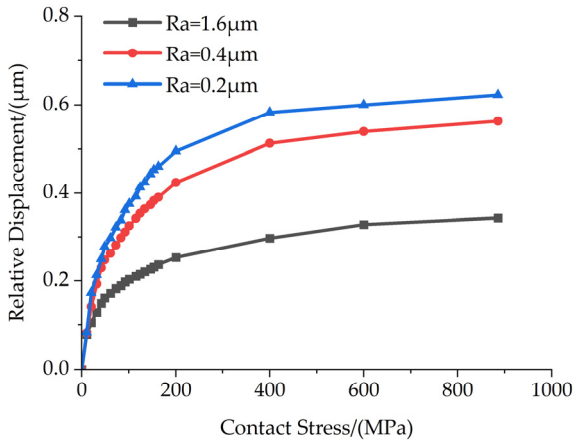


Figure 14. Relative displacement of rough surface affected by contact stress variation.

From a mechanical perspective, as the contact area expands, the effective contact stiffness of the surface increases, and the unit deformation of individual asperities begins to decrease. The involvement of more contact points not only distributes the overall load but also improves the uniformity of surface pressure, causing the localized deformation of the rough surface to stabilize over time. This process marks the transition of the contact interface from an initially uneven state to a more uniform load-bearing condition.

When the contact interface approaches a more uniform state, the trend of displacement growth gradually stabilizes. This phenomenon suggests that the compression deformation of rough asperities reaches a limit, beyond which further increases in contact stress no longer significantly alter the axial displacement. At this stage, the contact surface enters a relatively stable deformation and load-bearing state, which not only reflects the regularity of rough surface deformation but also provides a theoretical basis for contact interface design.

Furthermore, surface roughness plays a crucial role in contact behavior. Lower surface roughness (i.e., a smaller Ra value) results in a smoother surface with fewer asperities involved in contact. Under the same contact stress, more contact points contribute to load distribution, thereby improving the overall load-bearing performance. Additionally, smoother surfaces can distribute stress more evenly, reducing localized deformation and significantly lowering relative displacement.

In practical sealing cycles, the sealing surface undergoes wear due to friction. As the number of operating cycles increases, the wear causes the surface roughness to gradually increase from its initial state. This increase in roughness can lead to a higher leakage rate compared to the initial state, potentially resulting in a reduced valve maintenance cycle and increased operational and maintenance costs in industrial production. Therefore, it is essential to fully consider this factor during valve design and operation. This highlights the significant impact of wear-induced changes in surface roughness on sealing performance, which cannot be ignored in long-term use.

5. Experimental Analysis

5.1. Experimental Setup

As shown in Figure 15, the leakage rate testing setup for the elastic metal sealing ring is capable of measuring the helium leakage rate of the metal sealing ring under different axial loads and surface roughness conditions, corresponding to the all-metal angle valve. This setup simulates the sealing performance of the elastic metal sealing ring under real operating conditions. The leakage rate testing apparatus used is the PHOENIX Quadro model from LEYBOLD, Germany. This machine can be directly connected to the DN40 all-metal angle valve used in this study. If leakage rate testing for other valve models is required, the apparatus can be connected via an adapter pipeline for testing. This setup simulates the sealing performance of the elastic metal sealing ring under real operating conditions. The experimental system primarily consists of the test apparatus, a helium tank, and a helium mass spectrometry vacuum leak detection system, which are used to systematically measure the sealing performance of the sealing ring under complex working conditions.

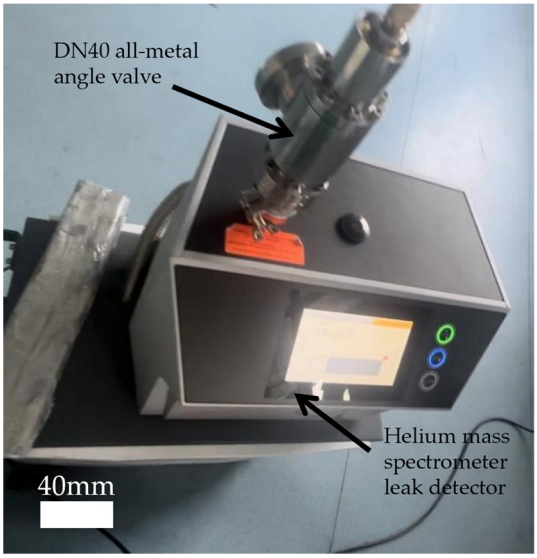


Figure 15. Experimental setup for leakage rate testing of metal sealing ring.

5.2. Experimental Procedure

(1) Preparation of Experimental Equipment

First, we assembled all components of the valve, except for the sample to be tested, and we placed the assembled valve body on the leak detection workstation. Next, we connected the valve assembly to the helium mass spectrometer vacuum leak detection system using the appropriate connecting parts, ensuring the sealing performance of the testing setup and the stability of the operation to guarantee the reliability of the experimental data.

(2) Equipment Inspection and Workbench Cleaning

We checked the operational status of all experimental equipment and instruments to ensure they were in normal working mode. Simultaneously, we cleaned the workbench to remove any debris, oil, or other contaminants that may interfere with the accuracy of the experiment, ensuring a clean experimental environment and standardized testing process.

(3) Preliminary Test Installation

We correctly installed Sealing Sample 1 into the valve body to be tested, ensuring the installation position was accurate and secure. Then, we closed the ultra-high vacuum angle valve and started the vacuum pump and leak detector at room temperature to enter the vacuum leak detection state.

(4) Leakage Testing

When the leak detector showed that the system vacuum had reached a level lower than 1×10^{-10} Pa, a helium gas gun was used to blow helium gas around the all-metal angle valve. The leakage rate displayed on the leak detector was closely monitored to determine whether any abnormal leakage occurred. If no abnormal leakage was detected, the leakage rate data were recorded, and the test for the Sample 1 sealing ring was considered complete.

(5) Sample Replacement and Repeat Testing

We shut down the testing equipment and replaced Sealing Sample 1 with Sealing Samples 2 and 3, ensuring that the replacement process caused no damage or contamination. We repeated the testing process according to steps (3) and (4), recording the leakage rate data for Sealing Samples 2 and 3.

5.3. Experimental Data and Analysis

A vacuum leak test was conducted following the leak detection test procedure at a constant load of 2.2 MPa under ambient conditions at 20 °C. The experiment was carried out in a temperature and humidity-controlled environmental chamber. The temperature was maintained at 20 °C using a high-precision temperature control system, with fluctuations kept within ±0.2 °C. Humidity was regulated using specialized dehumidification and humidification equipment, maintaining a relative humidity of 50%, with fluctuations controlled within ±5%. These controlled environmental conditions ensured that the influence of ambient conditions on the metal sealing performance remained within a manageable range. During the test, the leakage rates of sealing structures with sealing rings of different surface roughness values were measured to analyze the effect of surface roughness on sealing performance.

The uncertainty in the leakage rate measurement primarily arose from the accuracy error of the measuring instruments. The PHOENIX Quadro, used in the test, has a measurement error of ±0.5%. Additionally, slight fluctuations in environmental temperature could also influence the measurement results. To ensure the repeatability of the measurements, the instruments were calibrated according to the standard operating procedure before each measurement. Over 10 measurements were conducted on the same specimen, and the relative standard deviation of the results was maintained within ±0.3%. The results of the surface morphology observation and sealing performance tests for the three metal sealing specimens are summarized in Table 4.

Table 4. Surface roughness and leakage rate corresponding to three test samples.

Experimental Sample	Ra/μm	Helium Leakage Rate/(Pa·m^3/s)
Sample 1 (sealed)	1.6	1.41×10^{-9}
Sample 2 (sealed)	0.4	2.37×10^{-11}
Sample 3 (sealed)	0.2	1.28×10^{-11}

In the experiment, metal sealing rings with different surface roughness values exhibited significant differences in sealing performance.

These data indicate that as the surface roughness of the sealing ring decreases, the helium leak rate decreases significantly, resulting in a substantial improvement in sealing performance. The first metal sealing specimen did not meet the ultra-high vacuum (UHV) equipment requirements, with a leak rate an order of magnitude higher than those of the second and third specimens, which met the UHV standards. A comparative analysis of the microscopic rough surfaces corresponding to $L(He)_1$, $L(He)_2$, and $L(He)_3$ under the same load level revealed that metal sealing rings with lower roughness values generate more microscopic contact areas, thus significantly enhancing sealing performance. These results

suggest that reducing the surface roughness of metal sealing rings is a key approach to improving sealing performance.

6. Conclusions

(1) A finite element model of the DN40 all-metal angle valve was established, revealing that the equivalent stress and contact stress of the sealing ring are symmetrically distributed about the geometric center and increase linearly with the axial load applied to the valve head. Additionally, after contact is established, the sealing ring undergoes a counterclockwise rotation, leading to a contact area variation of less than 0.5% with the valve head taper, which remains relatively stable.

(2) The Weierstrass–Mandelbrot function was employed in MATLAB to generate point cloud data with different surface topographies. Using the non-uniform rational B-spline (NURBS) method, a three-dimensional rough surface model of the metal sealing ring was developed in CATIA. Subsequently, a preload model incorporating rough surface morphology was developed in ABAQUS using appropriate simplifications.

(3) The influence of surface roughness on the sealing performance of the elastic metal sealing ring was systematically validated by integrating experimental data. The results indicate that reducing the surface roughness to 0.2 μm enhances sealing performance by 45.9% compared to the 0.4 μm sealing ring, demonstrating significant superiority over the 1.6 μm sealing ring. The experimental findings align well with theoretical predictions.

(4) Further analysis reveals that reducing surface roughness significantly increases the effective contact area between the sealing ring and the valve head taper, thereby reducing leakage and improving sealing performance. Future research may explore the evolution of sealing performance under different material combinations, particularly in complex conditions such as high temperature, high pressure, and cyclic loading. Broadening the applicability of these conclusions will further strengthen the comprehensiveness and depth of this research. This study offers theoretical support for optimizing high-performance metal sealing structures and lays a foundation for the application of angle valves in high-end equipment manufacturing, aerospace, and ultra-high vacuum systems.

Author Contributions: Conceptualization, Q.Y. and Y.W.; methodology, Q.Y. and Y.W.; software, Q.Y. and Y.W.; validation, Q.Y. and Y.W.; formal analysis, Y.W.; investigation, Y.W.; resources, Q.Y.; data curation, Q.Y.; writing—original draft preparation, Q.Y. and Y.W.; writing—review and editing, Q.Y. and Y.W.; visualization, Q.Y. and Y.W.; supervision, Q.Y.; project administration, Q.Y. and Y.W.; funding acquisition, Q.Y. All authors have read and agreed to the published version of the manuscript.

Funding: This research was funded by Provincial Key Research Project of Natural Sciences in Universities of Anhui Province, grant number KJ2019A0796.

Data Availability Statement: The original contributions presented in this study are included in the article. Further inquiries can be directed to the corresponding author.

Conflicts of Interest: The authors declare no conflict of interest.

References

1. Hu, G.; Wang, G.; Dai, L.; Zhang, P.; Li, M.; Fu, Y. Sealing Failure Analysis on V-Shaped Sealing Rings of an Inserted Sealing Tool Used for Multistage Fracturing Processes. *Energies* **2018**, *11*, 1432. [CrossRef]
2. Thorness, R.B.; Nier, A.O. All-Metal Valve for Ultra-High Vacuum Use. *Rev. Sci. Instrum.* **1961**, *32*, 807–810. [CrossRef]
3. Xu, Y.; Wang, W.; Ming, Y.; Li, F.D.; Jin, H.Z. The Impact of Inlet Flash Evaporation Conditions on Erosion Damage Characteristics of Coal Gasification Black Water Angle Valve and Prevention Strategies. *Mech. Ind.* **2020**, *21*, 92. [CrossRef]
4. Kim, G.H.; Lee, Y.S.; Yang, H.L. A New Design Concept of Metal O-Ring Seal for Long-Term Performance. *Vacuum* **2016**, *123*, 54–61. [CrossRef]

5. Sang, Y.; Wang, X.; Sun, W.; Liu, P. Numerical and Experimental Study on the Friction of O-Ring for Hydraulic Seals. *Aust. J. Mech. Eng.* **2021**, *19*, 328–340. [CrossRef]
6. Zhou, Y.; Feng, H.; Zhang, S.; Zhuang, M.; Zhao, Z. Design and analysis of the inlet valve for the CFETR torus cryopump. *Energies* **2023**, *16*, 3107. [CrossRef]
7. Wang, Y.; Luo, W.; Liu, S.; Feng, H.; Li, J.; Wang, J. A model for reliability assessment of sealing performance of the C-shaped metal sealing ring at the outlet of the subsea tubing hanger. *Ocean Eng.* **2022**, *243*, 110311. [CrossRef]
8. Kim, G.H.; Lee, Y.S.; Yang, H.L. Experimental verification of newly proposed design of metal O-ring seal. *Vacuum* **2021**, *184*, 109942. [CrossRef]
9. Gao, B.; Gao, H.; Dong, J.; An, Y.; Wang, C. Analysis of sealing performance of metal B-ring self-tightening structure. *Processes* **2022**, *10*, 1084. [CrossRef]
10. Cheng, H.; Chen, X.; Chen, X.; Liu, H. Research on key factors of sealing performance of combined sealing ring. *Appl. Sci.* **2022**, *12*, 714. [CrossRef]
11. Kim, G.H.; Lee, Y.S.; Yang, H.L. Compliant Mechanism Topology Optimization of Metal O-Ring. *Trans. Korean Soc. Mech. Eng. A* **2013**, *37*, 537–545. [CrossRef]
12. Yan, H.; Zhao, Y.; Liu, J.; Jiang, H. Analyses toward Factors Influencing Sealing Clearance of a Metal Rubber Seal and Derivation of a Calculation Formula. *Chin. J. Aeronaut.* **2016**, *29*, 292–296. [CrossRef]
13. Blanton, P.S.; Eberl, K.R. Performance Testing of Spring Energized C-Rings for Use in Radioactive Material Packagings Containing Tritium. In Proceedings of the 15th International Symposium on the Packaging Transportation of Radioactive Materials (PATRAM), Miami, FL, USA, 21–26 October 2007; pp. 21–26.
14. Tsujikawa, H.; Maruoka, S.; Koeda, M.; Uryu, S.; Funaba, K.; Shibanuma, K.; Kakudate, S.; Kanamori, N.; Tada, E.; Ohkawa, Y. Preliminary Studies on Large Metal-Sealed Gate Valves for the International Thermonuclear Experimental Reactor (ITER). *Vacuum* **1996**, *47*, 639–646. [CrossRef]
15. Huang, Q.; Li, X.; Zhu, J.; Zhou, X. Analysis of Sealing Performance of Combined Seal Structure with Metal C-Ring with Built-In Spring. *Vibroeng. Procedia* **2023**, *51*, 94–100. [CrossRef]
16. El Bahloul, E.M.; Aissaoui, H.; Diany, M.; Boudaia, E.; Mabrouki, M. Performance Analysis of a Pressurized Assembly with a Reinforced O-Ring. *Int. J. Fluid Power* **2023**, *24*, 625–642. [CrossRef]
17. Gu, Z.; Dai, Q.; Ma, C.; Huang, W.; Wang, X. Leakage Retardation of Static Seals via Surface Roughness and Wettability Modification. *Langmuir* **2024**, *40*, 1–12. [CrossRef]
18. Wu, M.; Yang, L.; Shen, H. The Influence of Micro Morphology on Leakage of Metal Seals in Hydraulic Component. In Proceedings of the 9th International Conference on Fluid Power and Mechatronics (FPM), Lanzhou, China, 18–21 August 2023; pp. 1–6. [CrossRef]
19. Gu, Z.; Dai, Q.; Huang, W.; Wang, X. Effect of Surface Topography and Roughness on the Leakage of Static Seals. *Surf. Topogr. Metrol. Prop.* **2024**, *12*, 1–15. [CrossRef]
20. Nurhadiyanto, D.; Choiron, M.A.; Haruyama, S.; Kaminishi, K. Optimization of New 25A-Size Metal Gasket Design Based on Contact Width Considering Forming and Contact Stress Effect. *Int. J. Mech. Mechatron. Eng.* **2012**, *6*, 671–675.
21. Gong, X.; Cai, J.; Zhang, Q.; Li, S. Elastoplastic Contact Finite Element Analysis of Metal W-Sealing Ring. *Lubr. Eng.* **2010**, *35*, 82–85.
22. Persson, B.N.J.; Bucher, F.; Chiaia, B. Elastic Contact between Randomly Rough Surfaces: Comparison of Theory with Numerical Results. *Phys. Rev. B* **2002**, *65*, 184106. [CrossRef]
23. Scaraggi, M.; Persson, B.N.J. Viscoelastic Contact Mechanics between Randomly Rough Surfaces. *arXiv* **2014**, arXiv:1406.7236. [CrossRef]
24. Persson, B.N.J. Leakage of Metallic Seals: Role of Plastic Deformations. *Tribol. Lett.* **2016**, *63*, 42. [CrossRef]
25. Haruyama, S.; Choiron, M.A.; Kaminishi, K. A Study of Design Standard and Performance Evaluation on New Metallic Gasket. In Proceedings of the 2nd Symposium on Digital Manufacturing (ISDM'09), Wuhan, China; 2009; pp. 107–113.
26. Nurhadiyanto, D.; Choiron, M.A.; Haruyama, S.; Kaminishi, K. Study on Material Removal of Double Abrasive Grains in Ultrasonic Assisted Abrasive Cloth Wheel of GH4169 Alloy Blade. *Sci. Rep.* **2024**, *14*, 31160. [CrossRef]
27. Zhou, Y.Q.; Feng, H.S.; Zhuang, M.; Qiang, Y.; Li, S.L.; Zhao, Z.Y. Reliability assessment of metal C-ring sealing performance for CFETR torus cryopump main valve. *Vacuum* **2025**, *233*, 113930. [CrossRef]
28. Huang, L.; Qiu, C.; Wang, Y.; Wu, M.; Ren, S.; Miao, C. Analysis of Tangential Leakage Flow Characteristics in a Variable Diameter Dual Circular Arc Vortex Compressor. *Appl. Sci.* **2024**, *14*, 2262. [CrossRef]
29. Peng, C. Performance Analysis and Structural Optimization of Metal Sealing Rings in Ultra-High Vacuum Valves. Master's Thesis, Sichuan University, Chengdu, China, 2021.
30. Campbell, P.; Abhyankar, S. Fractals, Form, Chance and Dimension. *Math. Intell.* **1978**, *1*, 35–37. [CrossRef]
31. Yan, W.; Komvopoulos, K. Contact Analysis of Elastic-Plastic Fractal Surfaces. *J. Appl. Phys.* **1998**, *84*, 3617–3624. [CrossRef]

32. Hu, Y.Z.; Tonder, K. Simulation of 3-D Random Rough Surface by 2-D Digital Filter and Fourier Analysis. *Int. J. Mach. Tools Manuf.* **1992**, *32*, 83–90. [CrossRef]
33. Wang, S.; Shen, J.; Chen, W.K. Determination of the Fractal Scaling Parameter from Simulated Fractal Regular Surface Profiles Based on the Weierstrass-Mandelbrot Function. In Proceedings of the STLE/ASME International Joint Tribology Conference, San Antonio, TX, USA, 23–25 October 2006. [CrossRef]
34. Al Akhras, H.; Elguedj, T.; Gravouil, A.; Rochette, M. Isogeometric Analysis-Suitable Trivariate NURBS Models from Standard B-Rep Models. *Comput. Methods Appl. Mech. Eng.* **2016**, *307*, 256–274. [CrossRef]

Disclaimer/Publisher's Note: The statements, opinions and data contained in all publications are solely those of the individual author(s) and contributor(s) and not of MDPI and/or the editor(s). MDPI and/or the editor(s) disclaim responsibility for any injury to people or property resulting from any ideas, methods, instructions or products referred to in the content.